scientific reports

Check for updates

OPEN

Aging-related cerebral microvascular changes visualized using ultrasound localization microscopy in the living mouse

Matthew R. Lowerison[1,2,5], Nathiya Vaithiyalingam Chandra Sekaran[1,3,5], Wei Zhang[1,2,4], Zhijie Dong[1,2], Xi Chen[1,2], Daniel A. Llano[1,3]✉ & Pengfei Song[1,2]✉

Aging-related cognitive decline is an emerging health crisis; however, no established unifying mechanism has been identified for the cognitive impairments seen in an aging population. A vascular hypothesis of cognitive decline has been proposed but is difficult to test given the requirement of high-fidelity microvascular imaging resolution with a broad and deep brain imaging field of view, which is restricted by the fundamental trade-off of imaging penetration depth and resolution. Super-resolution ultrasound localization microscopy (ULM) offers a potential solution by exploiting circulating microbubbles to achieve a vascular resolution approaching the capillary scale without sacrificing imaging depth. In this report, we apply ULM imaging to a mouse model of aging and quantify differences in cerebral vascularity, blood velocity, and vessel tortuosity across several brain regions. We found significant decreases in blood velocity, and significant increases in vascular tortuosity, across all brain regions in the aged cohort, and significant decreases in blood volume in the cerebral cortex. These data provide the first-ever ULM measurements of subcortical microvascular dynamics in vivo within the context of the aging brain and reveal that aging has a major impact on these measurements.

The U.S. population is aging, with the number of adults over the age of 65 expected to nearly double by the year 2050[1]. This aging population is more vulnerable to cognitive impairment and dementia[2–4], which represents an emerging public health crisis with wide-reaching implications for quality of life and the economic burden of care[5]. However, aging-related cognitive decline remains a controversial area of research, with no established unifying mechanism identified for the cognitive and memory impairments seen in an aging population. Two of the most commonly observed pathological findings in the aged brain, both in human and in animal models, is decreased microvascular density and increased vessel tortuosity[6–12]. These findings imply that there is a relationship between compromised cerebral blood flow and cognitive impairment, where there are paralleled deteriorations in both small vessel function and cognitive ability. This relationship is reinforced by overlapping epidemiological risk factors[13]; both late-stage cognitive decline and vascular disease are associated with diabetes[14], obesity[15], and hypertension[16]. Furthermore, clinical evidence suggests that microvascular changes accelerate clinical decline in cognitive impairment[17,18], and decreased macroscopic cerebral blood flow is associated with worsened cognitive performance in both normal and pathological states[19–21].

However, the vascular hypothesis of cognitive decline remains difficult to test within a clinical context, given the requirement of high-fidelity microvascular imaging resolution in conjunction with a broad and deep brain imaging field of view – an undertaking that is fundamentally limited by the inherent trade-off of imaging penetration depth and resolution. The aging-associated decreases in cerebral microvascular density are heterogenous across brain regions[12,22,23], implying a selective vascular vulnerability that requires an imaging modality that

[1]Beckman Institute for Advanced Science and Technology, University of Illinois at Urbana-Champaign, Urbana, IL, USA. [2]Department of Electrical and Computer Engineering, Beckman Institute for Advanced Science and Technology, University of Illinois at Urbana-Champaign, 405 N. Mathews Ave, Urbana, IL 61801, USA. [3]Department of Molecular and Integrative Physiology, Beckman Institute for Advanced Science and Technology, University of Illinois at Urbana-Champaign, 405 N. Mathews Ave, Urbana, IL 61801, USA. [4]Department of Medical Ultrasound, Tongji Hospital, Tongji Medical College, Wuhan City, Hubei Province, China. [5]These authors contributed equally: Matthew R. Lowerison and Nathiya Vaithiyalingam Chandra Sekaran. ✉email: d-llano@illinois.edu; songp@illinois.edu

provides a broad field of view, high depth of penetration, and high spatial resolution. Traditional approaches in animal studies include histological analysis of the microvasculature, which does not provide information about the dynamics of blood flow. Multiphoton imaging may be applied to the surface of the brain to measure dynamics but cannot be applied to deep brain regions without the use of tissue-destructing prisms, periscopes, or fibers. Macroscopic blood flow measurement techniques such as single-photon emission computed tomography (SPECT) or MRI-based methods do not provide adequate spatial resolution to measure microscopic blood flow dynamics.

A recently proposed ultrasound-based super-resolution imaging modality, ultrasound localization microscopy (ULM)[24–27], can potentially address the need for microvascular imaging fidelity simultaneously with deep brain imaging. ULM processing leverages an intravascular injection of clinically used microbubble contrast agent to function as an imaging point target to break the diffraction limit of ultrasound. This technique can improve the vascular imaging resolution by a factor of about ten[28] over conventional ultrasound imaging, but does not sacrifice the imaging penetration depth, thereby side-stepping the classical compromise between imaging resolution and imaging depth. This improvement results in the ability to produce microvascular network reconstructions, potentially down to the capillary scale, that can cover an entire cross-section of the brain. Indeed, several research groups have demonstrated high-quality ULM images of the entire depth of the brain[26,29–31], but so far the application of the technique within the context of aging is unexplored. ULM also retains the non-invasiveness and safety profile of conventional contrast-enhanced ultrasound imaging.

In this report, we apply super-resolution ULM imaging to a mouse model of aging and quantify differences in cerebral vascularity, blood velocity, and vessel tortuosity across several brain regions captured across two coronal planes. Brain regions were chosen to examine the ability of ULM to image the vasculature in both superficial and deep structures. A total of 16 young (average age in weeks = 27.7; 8 female) and 11 aged (average age in weeks = 106.8; 7 female) mice of either sex were used in this study. Ultrafast (1000 Hz frame rate) contrast-enhanced ultrasound data were acquired using a Verasonics Vantage 256 ultrasound system and a L35-16vX high-frequency linear array transducer through a cranial window. ULM images were reconstructed at a 4.928 μm isotropic axial/lateral resolution. We found a reduction in cortical vascularity in the aged mouse group, and significant decreases in blood velocity and increases in tortuosity across multiple anatomical regions in comparison to the young mouse group. These data provide the first-ever ULM measurements of subcortical microvascular dynamics in vivo within the context of the aging brain and reveal that aging has a major impact on these measurements.

Results

Ultrasound imaging through cranial window allows simultaneous observation of multiple cortical and subcortical structures. The unilateral cranial window opened in this mouse cohort extended from the sagittal suture to the lateral aspect of the skull and was centered around 3 mm caudal from bregma (Fig. 1A). Extending the cranial window beyond the sagittal midline of the skull was avoided to prevent damage to the sagittal sinus, as this large blood vessel is sensitive to puncture from the Dremel tool used to remove the skull. This placement exposed the hemisphere of the mouse brain that contained both the auditory cortex and the auditory thalamus. Elevational tissue motion was minimal after securing the mouse via ear bars to the stereotaxic frame (Fig. 1B), however some respiratory motion was still present in the acquired contrast-enhanced in-phase/quadrature (IQ) dataset. Given that this motion was predominantly in-plane, it could be accounted for via 2D normalized cross-correlation. An example B-mode and power Doppler image (Fig. 1C) demonstrate the relevant anatomies of interest, with imaging penetration extending to the bottom of braincase. The diffraction-limited power Doppler image reveals highly vascularized brain tissue with an evident hierarchical vascular branching morphology. The corresponding Allen Brain Atlas[32] coronal section (Fig. 1D) with the ROIs highlighted shows a good correspondence to the ultrasound imaging field of view.

ULM processing permitted high-fidelity vascular mapping through the whole brain depth. Ultrafast planewave imaging of the mouse brain following contrast microbubble injection demonstrated a highly enhancing vascular bed along with the strong acoustic backscatter from tissue (Fig. 2A). The flowing microbubble signal could be extracted from the tissue background by applying SVD clutter filtering (Fig. 2B), and the microbubble signal intensity needed to be normalized using a noise equalization profile[33] before any upstream processing. This image processing yielded isolated microbubble signal at a high concentration, which was split into sparser datasets using a microbubble separation filter[29]. The microbubbles in these sparser subsets could then be localized by detecting their centroids (Fig. 2C), producing centroid coordinate vectors that can serve as input into the uTrack algorithm for pairing and tracking. Super-resolution ULM images from each data subset (Fig. 2D) demonstrated the reconstruction of different vascular features, which depend on the flow direction, velocity, and decorrelation of the microbubble signal. The combination of each of these ULM subset reconstructions resulted in an accumulation image (Fig. 2E) with a high degree of vascular perfusion given the relatively short imaging period (1600 frames, or 1.6 s of acquisition). The final ULM reconstruction used 80 of these accumulation maps (128 s of data) to ensure that the majority of the microvascular bed had been perfused with microbubbles[34–36].

ULM reconstructions of young and aged mouse brains reveal distinct vascular phenotypes. A representative example comparison of a young mouse brain and an aged mouse brain (Fig. 3A) demonstrate several key observations of the cerebral vasculature. In both cases, the cerebral cortical microvasculature comprises a distinct layer of columnar vessels perpendicular to the cortex, reaching from the brain surface to the subcortical border. Generally, the young cortex demonstrates more densely packed microvasculature with a more orderly

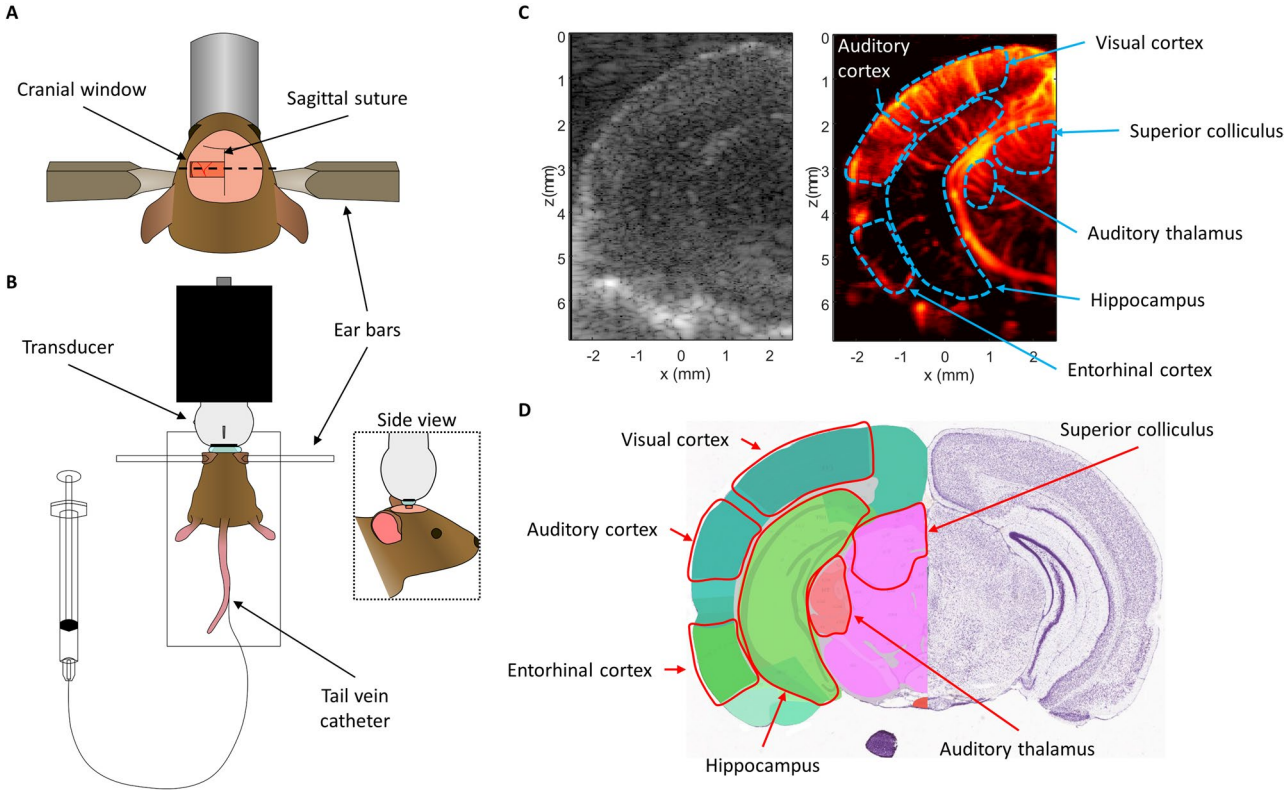

Figure 1. Ultrasound imaging acquisition through cranial window. (**A**) A rectangular cranial window was opened in the mouse skull spanning from the sagittal suture to the lateral side of the skull, centered approximately 3 mm away from bregma. This exposed the auditory cortex and auditory thalamus for ultrasound imaging. (**B**) Diagrammatic example of the stereotaxic imaging frame. The mouse was positioned on a heated pad and the skull was secured to the stage using ear bars. The high-frequency ultrasound transducer was connected to a linear translation motor via a custom 3D printed holder. Tail-vein catheterization permitted controlled and repeatable bolus injections of microbubble contrast agent. (**C**) Representative B-mode and power Doppler (no contrast) images from the first imaging plane. The ROIs used in this study (auditory cortex, auditory thalamus, entorhinal cortex, superior colliculus, and visual cortex) are outlined in blue. B-mode and power Doppler images were rendered using MATLAB (R2019a, https://www.mathworks.com/). (**D**) Mouse coronal section taken and modified from the Allen Brain Atlas [32] shows good correspondence between the features seen in the B-mode and power Doppler image with the anatomies of interest.

structure, whereas the aged brain cortex demonstrates some regional hypo-perfusion and a more disorganized appearance. The hippocampal and thalamic regions generally demonstrate similar levels of overall blood perfusion in both the young and aged brain; however, the older cohort exhibits a more stratified distribution of apparent microvascular velocities with a higher proportion of fast microbubble signal appearing in the large vessels. By contrast, the young mouse hippocampal and thalamic microvessels have a more gradual shift from the fast microbubble velocities in large vasculature to the slower microbubble events in the small vasculature. We attempted to quantify this difference in the apparent cerebral vascular distribution by using a K-means clustering algorithm on the super-resolution vessel density maps (Fig. 4A) to independently analyze the larger and smaller vessels within each image (Fig. 4B). No significant difference was found between the young and aged cohort for either the arteriole/venule intervessel distance or ULM small vessel density (Fig. 4C). However, we did find a significantly increased right skewness (1.16 vs. 0.98, $p = 0.002$) of the distribution of blood velocities across the whole depth of the brain in the aged cohort versus the young cohort. A representative example of a histogram of blood velocities for a young and aged mouse is demonstrated in Fig. 4D.

Aged mice have quantitatively different vasculature than young mice. The aged and young mouse cohorts were quantitatively compared based on super-resolution ULM measurements of their auditory cortex, auditory thalamus, entorhinal cortex, hippocampus, superior colliculus, and visual cortex (Fig. 5). Blood volume was estimated using the mean number of microbubbles that entered a particular ROI. The auditory cortical blood volume (Fig. 5A) of the aged mouse group was significantly lower than the young mouse group ($p < 0.001$) and no significant differences were seen in the auditory thalamus or hippocampus. The blood volume was also found to be significantly decreased in the entorhinal cortex ($p = 0.007$) and the visual cortex ($p = 0.001$). Similar observations can made about the vascularity of the young brain versus the aged brain (Fig. 5B), where a significant decrease in vascularity was only found for the auditory cortical ($p = 0.018$) and visual cortical ($p = 0.02$)

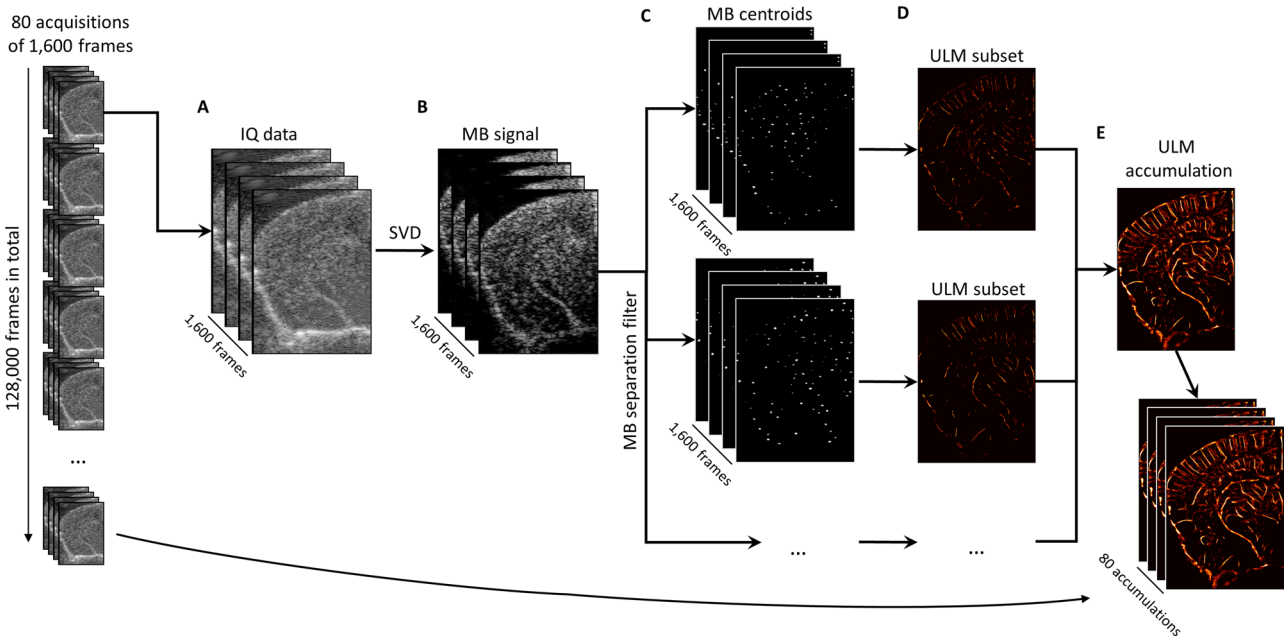

Figure 2. Super-resolution reconstruction workflow. (**A**) Each 1,600 frame IQ data acquisition was represented as a 3D matrix of stacked imaging frames. This was then reshaped into a Casorati matrix and an (**B**) SVD filter was applied to extract the moving microbubble signal from the highly spatiotemporally coherent tissue background. (**C**) A microbubble separation filter was then applied to split the high concentration microbubble dataset into sparser subsets, each of which were independently processed. The microbubble locations were detected on each subset using a 2D normalized cross-correlation with an empirically determined PSF function. (**D**) The uTrack algorithm was then applied on detected centroids to pair microbubbles and estimate trajectories. (**E**) The final reconstruction for this 1,600 frame dataset was produced by combining each of the independently processed data subsets. Images were rendered using MATLAB (R2019a, https://www.mathworks.com/).

ROIs. Regional blood velocity demonstrated a significant decrease across all of the measured brain regions in the aged mouse group in comparison to the young mouse group (Fig. 5C). The effect was the most pronounced in the superior colliculus ($p < 0.001$) and visual cortex ($p < 0.001$), with proportionally lowered reduction in velocity for the hippocampal, thalamic, auditory cortical, and entorhinal cortical ROIs ($p = 0.015$, $p = 0.003$, $p = 0.004$, and $p = 0.001$, respectively). The tortuosity of brain vasculature was estimated using the Sum of Angles Metric (SOAM), which has been previous described by Shelton et al.[37]. A diagrammatic example detailing the metric is demonstrated in Fig. 3B. All of the measured brain regions had significantly higher metrics of SOAM tortuosity in the aged mouse group in comparison to the young group (Fig. 5D). Specifically, we found significant SOAM increases in the auditory cortex ($p = 0.004$), auditory thalamus ($p = 0.006$), entorhinal cortex ($p = 0.001$), hippocampus ($p = 0.041$), superior colliculus ($p = 0.002$), and visual cortex ($p < 0.001$). This difference in vessel structural organization, specifically the SOAM metric, mirrors the age-associated decreases in blood velocity that were seen in these anatomical regions. The quantification of contrast power on diffraction-limited contrast-enhanced images did not demonstrate any significant differences between the brain regions (Supplementary Fig. 1). Colorflow imaging found a significant increase only in hippocampal blood velocity in the aged cohort ($p = 0.026$).

Multivariate linear regression analyses on the four ULM quantification metrics with mouse age and mouse sex as independent variables are presented in Supplementary Tables 1, 2, 3, 4. Animal sex was found to have a significant impact on the blood volume in the entorhinal cortex (Supplementary Table 2), and on the SOAM in the hippocampus (Supplementary Table 4).

Discussion

This study quantified aging-associated changes in the cerebral microvasculature using super-resolution ULM imaging in a mouse model of aging. We demonstrated that ULM imaging provides access to microvessel structural and functional information throughout the entire depth of a coronal section of the brain, allowing for the simultaneous observation of several distinct superficial and deep anatomical brain regions. This ability to conduct global brain imaging is critical for detecting and quantifying the selective vascular vulnerability that is hypothesized to contribute to the heterogeneous decreases in aging-associated cerebral microvascular density[12,22,23].

We found that the aged brain demonstrated decreases in the cortical vascular density and blood volume as measured by ULM imaging (Figs. 3 and 5). This finding is consistent with the literature, which reports that aging is associated with decreases in histological and functional measurements of microvascular density throughout the cerebral blood supply[6–12,38]. A more profound effect was observed when comparing the mean blood flow velocity and vascular tortuosity of the aged cohort versus the young mouse group. We also found global

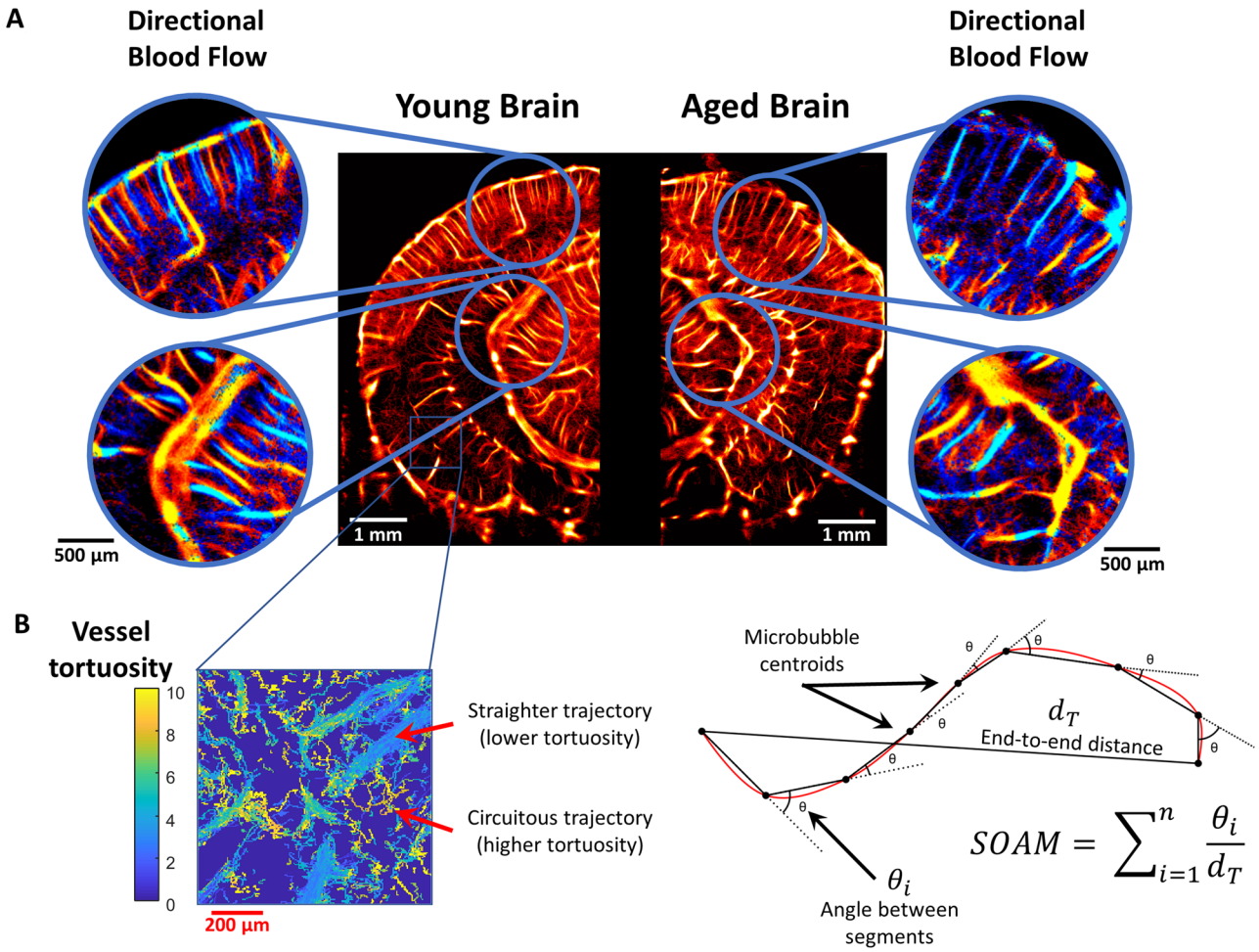

Figure 3. ULM imaging of young and aged mouse brain. (**A**) Example ULM microvessel density maps images from a (left) young mouse brain and (right) an aged mouse brain. Local cortical and subcortical regions are selected and magnified to show the corresponding directional blood flow maps (blue toward the transducer, red away from the transducer). (**B**) An inset image demonstrating distinct vessel tortuosity phenotypes. The larger, straighter vessels have a relatively low measured tortuosity, whereas the smaller connecting vessels are more circuitous. A diagrammatic example of how the sum of angles metric was determined using the microbubble trajectory data. For each complete microbubble trajectory the total path length, end-to-end distance, and angle between every segment was used in the calculation. ULM images were rendered using MATLAB (R2019a, https://www.mathworks.com/).

decreases in flow velocity and global increases in tortuosity across all analyzed brain regions of the aged mice. This functional decrease in aging-associated cerebral blood flow is a more direct indicator of impaired vascular supply than inferring such impairments from histological findings which indicate reduced microvascular density. Consistent with previous work on regional brain metabolism and regional brain blood flow[39–42], of the measured brain regions, the neocortex had the highest blood volume and vascularity. Neocortex also showed the most significant aging-related drops in blood volume and vascularity, consistent with previous work demonstrating cortical vulnerability during the aging process[43,44].

A possible explanation for the decrease in mean velocity for the aged cohort is a consequence of aging-related deficits in cerebral blood flow pulsatility[45]. However, the long imaging duration of ULM acquisitions functions as a temporal averaging of blood velocity during the cardiac cycle, and thus obscures the influence of pulsatility on blood flow. The 128-s total imaging duration for each imaging plane in this study will include hundreds of mouse cardiac cycles, and so we do not anticipate a bias in cardiac cycle sampling in the final ULM reconstructions. New technical developments for ULM processing, such as deep-learning based approaches to velocity estimation[46], could allow for more direct observation of microvascular pulsatility, but this is outside of the scope of the current study. Intuitively, the circuitous blood vessel structures (Fig. 3B) that are measured using the SOAM metric should lead to increased resistance to blood flow and corresponding regional inefficiencies in blood delivery. This measured difference in vessel structural organization is also reflected in the age-associated decreases in blood velocity observed in anatomical regions throughout the brain. Diffraction-limited contrast-enhanced ultrasound image was found to be insensitive to the aging-related shifts in brain vascularization (Supplementary Fig. 1). A possible explanation is that ULM processing, due to the strict microbubble localization and tracking

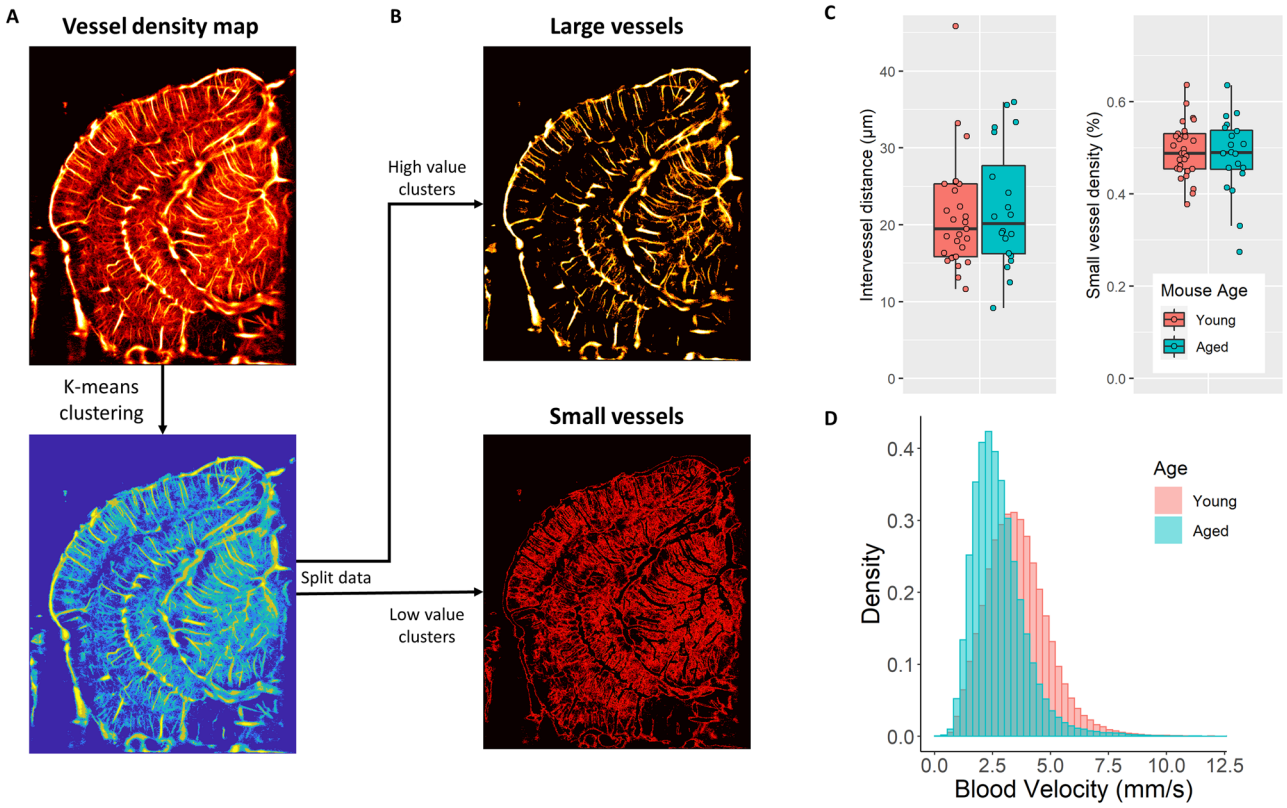

Figure 4. ULM image clustering and distributional analysis. (**A**) Super-resolution vessel maps were clustered based on microbubble accumulation density using K-means clustering with 6 clusters. (**B**) Splitting the clustered map into separate high-valued and low-valued images allowed for the generation of large vessel and small vessel representations of the ULM data, respectively. (**C**) The mean intervessel distance across the entire coronel hemisphere for the large vessel map could be calculated, along with the microvascular density for the small vessel map, for all mice in each age group. No significant difference was found between the age groups for either of these metrics. (**D**) Representative histograms of the blood velocities across the entire coronel hemisphere from an example young and aged mouse, demonstrating a shift in the distribution shape. Across all mice in this study, we found a significantly increased right skewness (1.16 vs. 0.98, $p = 0.002$) in the distribution of blood velocities of the whole brain in the aged cohort versus the young cohort. ULM images were rendered using MATLAB (R2019a, https://www.mathworks.com/).

requirements, is more robust to the sources of variability that lead to the inconsistent quantification performance of conventional contrast-ultrasound[47]. Furthermore, ULM velocity estimation is performed via frame-to-frame tracking of individual microbubbles, as opposed to the Doppler frequency shift as in colorflow imaging, and is thus less susceptible to Doppler angle dependence. It is also better able to estimate velocity in small vessels where the Doppler shift is small.

Similar findings of decreased velocity and increased tortuosity have also been reported in literature using other imaging modalities. Murugesan et al.[48] used confocal microscopy to perform regional brain microvessel density and branching analysis on the cortex, hippocampus, and subcortical white matter (corpus callosum) of young vs. aged mice. They found significant decreases in the capillary density across all regions, and significant decreases in branching in the cortex and white matter, but not the hippocampus, in aged mice. Faber et al.[49] found that a tortuosity index in the cerebral collateral vessels in mice was significantly increased as early as 16 months of age, with an increasing relative resistance to blood flow as the mice matured. Kang et al.[50] performed fluorescent imaging on groups of young 2-month old and aged 12-month old mice, finding that the aged cohort had reduced brain blood flow and more curved pial arteries. They also found that the peak fluorescent intensity and blood flow index was decreased, and mean transit time was increased, in the middle cerebral artery and superior sagittal sinus of the aged mice. Taken together, these results corroborate our findings that healthy aging in the mouse brain is typified by increasing vascular tortuosity, and decreasing mean blood velocity, across several anatomical regions. Interestingly, females were found to have an increased blood volume in the entorhinal cortex and increased vessel tortuosity in the hippocampus (Supplementary Tables 2 and 4, respectively). Also, when also accounting for sex differences between mice, our measure of vascular tortuosity in the hippocampus was no longer found to reach the threshold of statistical significance between young and aged mice. These data are consistent with previous work demonstrating increases in hippocampal and entorhinal cortex blood flow tied to estrogen levels[51–54]. Future work should also include in-depth consideration for any sex-based and estrus cycle-based differences in cerebral vasculature and neurodegeneration.

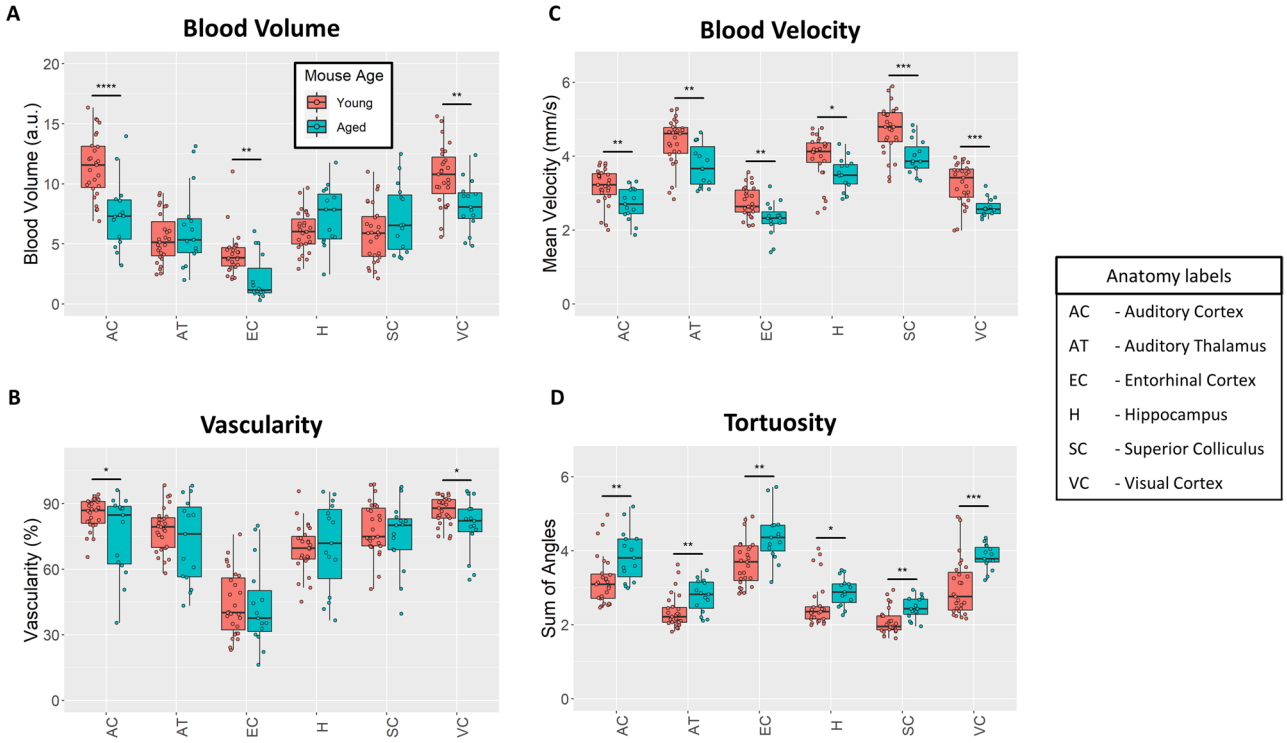

Figure 5. Quantitative ULM measurements. (**A**) Cortical blood volume was significantly decreased in the aged mouse group in comparison to the young group ($p < 0.001$ for the auditory cortex, $p = 0.007$ for entorhinal cortex, and $p = 0.001$ for visual cortex). (**B**) Likewise, ULM measured vascularity demonstrated a significant decrease in the auditory cortex and visual cortex of the brain between the aged and young group ($p = 0.018$ and $p = 0.02$, respectively). (**C**) Blood velocity exhibited global decreases across all measured brain regions in the aged mouse cohort. The superior colliculus ($p < 0.001$) and visual cortex ($p < 0.001$) demonstrated the most substantial decrease in mean velocity, with proportionally less decrease in the hippocampus ($p = 0.015$), auditory thalamus ($p = 0.003$), auditory cortex ($p = 0.004$), and entorhinal cortex ($p = 0.001$). (**D**) Vascular tortuosity, as measured by sum of angles metric, showed significant increases across all brain regions ($p = 0.004$ for auditory cortex, $p = 0.006$ for auditory thalamus, $p = 0.001$ for entorhinal cortex, $p = 0.041$ for hippocampus, $p = 0.002$ for superior colliculus, and $p < 0.001$ for the visual cortex).

Furthermore, an interesting observation from a direct comparison of super-resolution images of the young and aged mouse brain (Fig. 2) was the qualitative appearance of a more stratified distribution of microvascular velocities with a higher proportion of the relatively faster microbubble signal appearing in large vessels in the aged mouse brain. This manifested quantitatively as a significantly increased right skewness (1.16 vs. 0.98, $p = 0.002$) of the distribution of blood velocities of the whole brain in the aged cohort versus the young cohort, with the heavier tail implying a less gradual shift from slow flowing microvessels to faster arterioles (Fig. 4D). This observation mirrors the findings of Bell and Ball[12] who conducted a morphometric comparison of hippocampal microvessels in aging humans. They found that aging was associated with increases in the diameters of both capillaries and arterioles and, while the density of capillaries decreased, the density of arterioles increased significantly in the aged brain. It can be speculated that this shift in the proportion of vessel diameters in the aging brain should lead to a corresponding shift in blood flow velocities. A more direct comparison examining the distribution of ULM-determined vessel diameters with respect to age was attempted using a K-means clustering algorithm (Fig. 4), but no significant difference was found. A plausible explanation for this discordance with literature is that any difference in vessel size distributions may have been obscured by the relatively thick elevational beamwidth of ultrasound imaging. Furthermore, a substantial limitation of ULM is that the image reconstruction is stochastic. Vessel lumens are gradually filled in with sparse localizations of microbubble trajectories and without a priori knowledge of the vessel structure it is difficult to determine the fully perfused vessel diameters. Conventionally, the measurement of vessel sizes in ULM is done through a process of manual selection and segmentation, which is both laborious and prone to bias, and limits the generalizability of the analysis.

This study has some further limitations that should be addressed. ULM imaging is a relatively new technology that is still being optimized and many of the functional output metrics (such as velocity) lack a well-established gold-standard reference to confirm that the reconstructions are informative of the true physiology. We have previously found that ULM imaging in a tumor model correlated with histological measurements of microvascular density and that ULM measurements of tortuosity were informative of tissue hypoxia[55]. The choice of anesthesia could also impact the underlying physiology and therefore the quantifications of cerebral blood flow. In this study, we anesthetized the mice for imaging using vaporized isoflurane mixed with oxygen. However, it is well-established that isoflurane has a dose-dependent dilatory effect on the cerebral blood flow[56], which is

particularly problematic, as aged mice can become more sensitive to anesthesia. This uncertainty in the cerebral blood supply is also exacerbated by the requirement for long imaging acquisitions times in ULM imaging to ensure that the majority of the microvasculature has been perfused with microbubbles[34–36]. The ULM imaging protocol in this study typically requires that the mouse be under anesthesia for at least 2 h total to perform the craniotomy, secure the animal to the imaging stage, place the tail vein catheter, and to acquire the data. The long imaging duration is also a considerable challenge for the clinical translation of the technology, as any relative motion between the transducer and the patient will degrade ULM performance. Non-invasive clinical ULM imaging of the brain is particularly challenging due to the difficulties associated with transcranial ultrasound wave propagation, attenuation, and phase aberration. The sound speed and tissue density mismatch between the cranial bone and brain, combined with the heterogeneous structure of the human skull, lead to substantial distortions to the microbubble signal that result in high localization uncertainty. Thus far, successful ULM imaging of the human brain has only been demonstrated through the temporal window of the skull[31].

We have demonstrated that ULM imaging can provide subcortical microvascular dynamics in vivo to inform vascular phenotypes associated with the aging brain. Given the lack of tissue destruction and safety profile of ULM imaging, this technique lends itself well to longitudinal studies of cerebral blood flow to further examine pathological neurodegeneration and to elucidate vasculature-based mechanisms of neuroprotection. Longitudinal study design could either implement a chronic cranial window using an acoustically transparent plastic, such as polymethylpentene[57], or could conduct transcranial imaging with sophisticated phase-aberration correction[31,58]. Based on the current findings, a larger study examining the microvascular structure and function of additional cohorts of mouse ages is warranted.

Materials and methods

Animal model. All procedures on mice presented in this manuscript were approved by the Institutional Animal Care and Use Committee (IACUC) at the University of Illinois Urbana-Champaign (protocol # 19,063). All experiments were performed in accordance with the IACUC guidelines. Reporting in this manuscript follows the recommendations of the ARRIVE guidelines[59]. Mice were housed in an animal care facility approved by the Association for Assessment and Accreditation of Laboratory Animal Care. CBA/CaJ mice were bred in-house. A total of 16 young (8 female; average age in weeks = 27.7, max = 46.8, min = 11.6) and 11 aged (7 female; average age in weeks = 106.8, max = 126.9, min = 90.6) CBA/CaJ mice of either sex were used in this study.

Animal preparation for ultrasound imaging. Mouse anesthesia was induced using a gas induction chamber supplied with 4% isoflurane mixed with medical oxygen, and then mice were placed in a stereotaxic frame with nose cone supplying 2% isoflurane with oxygen for maintenance. Lidocaine (1%) was intradermally injected in the scalp to supplement anesthesia. Ear bars were used to secure the mouse head to the stereotaxic imaging stage. The scalp of the mouse was removed, and a cranial window was opened on the left side of the skull using a rotary Dremel tool, starting at the sagittal suture and moving laterally to expose the lateral expanse of the cerebral cortex. The tail vein of the mouse was cannulated with a 30-gauge catheter and vessel patency was confirmed with a 0.1 mL injection of sterile saline.

Ultrasound imaging. A Verasonics Vantage 256 system (Verasonics Inc., Kirkland, WA) was used for all ultrasound imaging in this study. A L35-16vX transducer (Verasonics) was secured via a 3D-printed transducer holder to a translation motor (VT-80 linear stage, Physik Instrumente, Auburn, MA) that was connected to the stereotaxic imaging frame. The transducer was then positioned above bregma, via visual inspection, oriented to produce a coronal anatomical section of the brain. Acoustic contact gel was applied directly to the surface of the mouse brain and adjacent skull, and the transducer was lowered into position. Once acoustic coupling was confirmed, the motorized stage was adjusted at 0.1 mm increments caudally to find an appropriate imaging plane which contained the auditory cortex and auditory thalamus. This was generally 3.0–3.5 mm caudal to bregma. The imaging field of view was then adjusted to cover the entire half of the mouse brain in this anatomical position, and a short 400-frame data acquisition was processed to produce a power Doppler image as in[60] to confirm transducer placement over the anatomy of interest (Fig. 1C). A clinically available ultrasound contrast agent (DEFINITY, Lantheus Medical Imaging, Inc.) was prepared by diluting 1.3 mL activated DEFINITY with 8.7 mL sterile saline. A 50uL bolus of contrast was injected into the mouse just prior to starting image acquisition. Imaging was performed with a center frequency of 20 MHz, using 9-angle plane wave compounding1-degree increments with a post-compounding frame rate of 1,000 Hz. Ultrasound data was saved as in-phase/quadrature (IQ) datasets for off-line processing in MATLAB (The MathWorks, Natick, MA; version R2019a). A fresh 50uL bolus of microbubbles was injected after every 10 imaging acquisitions 1,600 frames per acquisition. A total of 80 acquisitions (128,000 frames, or 128 s of data) was acquired for this imaging plane. The transducer was then moved 0.5 mm in the rostral direction, and the contrast microbubble imaging procedure was repeated for another 80 acquisitions at this second imaging plane, for a final total of 2×80 acquisitions for each mouse in this study.

Ultrasound signal processing and super-resolution reconstruction. The isolated microbubble signals were extracted from the contrast-enhanced IQ data by applying a spatiotemporal singular value decomposition (SVD)-based clutter filter[61,55,29,62]. Briefly, each IQ dataset was first reshaped into a columnized 2D Casorati matrix and an SVD decomposition was performed to reveal the singular values of the data. A low-order singular value threshold was determined adaptively[63] to filter out tissue signal, which typically zeroed out the first 10–20 singular values. An inverse SVD was then performed, and the data was reshaped into the original data size. A noise-equalization profile[33] was then applied to equalize the microbubble signal intensity through the entire

depth of imaging. Contrast signal power was calculated by accumulating the SVD-filtered microbubble signal in the diffraction-limited contrast images within each ROI along the temporal dimension. Contrast-enhanced color-flow images were calculated using the 2D autocorrelation technique detailed by Loupas et al.[64].

An isolated microbubble signal was manually identified, and a multivariate Gaussian function was empirically fit to the axial and lateral dimensions to represent the point-spread function (PSF) of the system. A microbubble separation filter[29] was then applied to the SVD-filtered IQ dataset to separate it into data subsets that have more spatially sparse microbubble distributions. Each IQ data subset was then spatially interpolated to an isotropic 4.928 μm axial/lateral resolution using 2D spline interpolation[65]. A normalized 2D cross-correlation was then performed with the empirical PSF to localize microbubbles on every frame. Pixels with a low cross-correlation coefficient were excluded via a threshold[29,55,66], and microbubble centroids were localized with the MATLAB built-in "imregionalmax.m" function. Frame-to-frame microbubble centroid pairing and trajectory estimation was performed using the uTrack algorithm[67]. A minimum microbubble trajectory length of 20 frames (i.e., 20 ms) was applied to the super-resolution reconstructions presented in this study. Inter-acquisition registration was performed on each of the individual 1,600-frame ULM accumulation using a 2D normalized cross-correlation, with the first ULM acquisition as the reference, before the final accumulation.

Ultrasound image analysis. Brain anatomical regions (auditory cortex, auditory thalamus, entorhinal cortex, hippocampus, superior colliculus, and visual cortex) were segmented by manually placing Bezier control vertices on the border of the region of interest (ROI) and by interpolating with Hobby's algorithm[68]. Brain vascularity was calculated by binarizing the super-resolution vessel maps to determine the percentage of cross-section that was perfused. Blood vessel velocity was determined for every microbubble track directly from the frame-to-frame displacement of detected microbubble centroids. The sum of angles metric, a measure of vascular tortuosity, was calculated for every microbubble trajectory using the algorithm described by Shelton et al.[37]. Large and small vessel segmentation was performed using K-means clustering with 6 clusters. Imaging plane data was excluded from analysis if the animal died prematurely during the acquisition. Under this criterion a total of 3 imaging acquisitions from aged mice (one male, two female) and 3 imaging acquisitions from young mice (one male, two female) were excluded from analysis.

Statistics. All statistical analysis was performed in the R programming language[69], and all graphs were generated using the ggplot2 package[70]. A two-way analysis of variance (ANOVA) was applied to test for statistical significance between young and aged mouse brain anatomy with a Tukey's honestly significant difference test applied as a post-test. A $p < 0.05$ was considered as statistically significant. Multivariate linear regression modeling was performed in R.

Data availability

The data that support the findings of this study are available from the corresponding authors on request.

Received: 19 August 2021; Accepted: 14 December 2021
Published online: 12 January 2022

References

1. Bureau, U.C. An Aging Nation: The Older Population in the United States [Internet]. The United States Census Bureau. [cited 2021 May 3]. Available from: https://www.census.gov/library/publications/2014/demo/p25-1140.html
2. Salthouse, T. A. Memory aging from 18 to 80. *Alzheimer Dis Assoc Disord.* **17**(3), 162–167 (2003).
3. Horn, J. L. & Cattell, R. B. Age differences in fluid and crystallized intelligence. *Acta Physiol. (Oxf)* **26**(2), 107–129 (1967).
4. Glisky, E. L. Changes in Cognitive Function in Human Aging. In *Brain Aging: Models, Methods, and Mechanisms* (ed. Riddle, D. R.) (CRC Press/Taylor and Francis, Boca Raton, 2007).
5. Jutkowitz, E. *et al.* Societal and family lifetime cost of dementia: implications for policy. *J. Am. Geriatr. Soc.* **65**(10), 2169–2175 (2017).
6. Sonntag, W. E., Lynch, C. D., Cooney, P. T. & Hutchins, P. M. Decreases in cerebral microvasculature with age are associated with the decline in growth hormone and insulin-like growth factor 1. *Endocrinology* **138**(8), 3515–3520 (1997).
7. Bell, M. A. & Ball, M. J. Neuritic plaques and vessels of visual cortex in aging and Alzheimer's dementia. *Neurobiol. Aging.* **11**(4), 359–370 (1990).
8. Desjardins, M., Berti, R., Lefebvre, J., Dubeau, S. & Lesage, F. Aging-related differences in cerebral capillary blood flow in anesthetized rats. *Neurobiol. Aging.* **35**(8), 1947–1955 (2014).
9. Brown, W. R., Moody, D. M., Thore, C. R., Challa, V. R. & Anstrom, J. A. Vascular dementia in leukoaraiosis may be a consequence of capillary loss not only in the lesions, but in normal-appearing white matter and cortex as well. *J. Neurol. Sci.* **257**(1–2), 62–66 (2007).
10. Casey, M. A. & Feldman, M. L. Aging in the rat medial nucleus of the trapezoid body. III. Alterations in capillaries. *Neurobiol. Aging.* **6**(1), 39–46 (1985).
11. Burns, E. M., Kruckeberg, T. W. & Gaetano, P. K. Changes with age in cerebral capillary morphology. *Neurobiol. Aging.* **2**(4), 285–291 (1981).
12. Bell, M. A. & Ball, M. J. Morphometric comparison of hippocampal microvasculature in ageing and demented people: diameters and densities. *Acta Neuropathol.* **53**(4), 299–318 (1981).
13. Papunen, S. *et al.* The association between diabetes and cognitive changes during aging. *Scand. J. Prim. Health. Care.* **38**(3), 281–290 (2020).
14. Ryan, C. M. Diabetes, aging, and cognitive decline. *Neurobio.l Aging.* **26**(Suppl 1), 21–25 (2005).
15. Nguyen, J. C. D., Killcross, A. S. & Jenkins, T. A. Obesity and cognitive decline: role of inflammation and vascular changes. *Front Neurosci* **8**, 375 (2014).
16. Hajjar, I., Goldstein, F. C., Martin, G. S. & Quyyumi, A. A. Roles of Arterial stiffness and blood pressure in hypertension-associated cognitive decline in healthy adults. *Hypertension* **67**(1), 171–175 (2016).
17. Solfrizzi, V. *et al.* Vascular risk factors, incidence of MCI, and rates of progression to dementia. *Neurology* **63**(10), 1882–1891 (2004).

18. Snowdon, D. A. *et al.* Brain infarction and the clinical expression of Alzheimer disease. *Nun Study. JAMA.* **277**(10), 813–817 (1997).
19. Gustafson, L. & Hagberg, B. Emotional behaviour, personality changes and cognitive reduction in presenile dementia: related to regional cerebral blood flow. *Acta Psychiatr. Scand. Suppl.* **257**, 37–71 (1975).
20. Brown, A. D. *et al.* Effects of cardiorespiratory fitness and cerebral blood flow on cognitive outcomes in older women. *Neurobiol. Aging.* **31**(12), 2047–2057 (2010).
21. Heo, S. *et al.* Resting hippocampal blood flow, spatial memory and aging. *Brain Res.* **1315**, 119–127 (2010).
22. Abernethy, W. B., Bell, M. A., Morris, M. & Moody, D. M. Microvascular density of the human paraventricular nucleus decreases with aging but not hypertension. *Exp. Neurol.* **121**(2), 270–274 (1993).
23. Mann, D. M., Eaves, N. R., Marcyniuk, B. & Yates, P. O. Quantitative changes in cerebral cortical microvasculature in ageing and dementia. *Neurobiol. Aging.* **7**(5), 321–330 (1986).
24. Couture, O., Besson, B., Montaldo, G., Fink, M., Tanter, M. Microbubble ultrasound super-localization imaging (MUSLI). In *2011 IEEE International Ultrasonics Symposium*. 1285–1287. (2011).
25. Viessmann, O. M., Eckersley, R. J., Christensen-Jeffries, K., Tang, M. X. & Dunsby, C. Acoustic super-resolution with ultrasound and microbubbles. *Phys. Med. Biol.* **58**(18), 6447–6458 (2013).
26. Errico, C. *et al.* Ultrafast ultrasound localization microscopy for deep super-resolution vascular imaging. *Nature* **527**(7579), 499–502 (2015).
27. Christensen-Jeffries, K., Browning, R. J., Tang, M.-X., Dunsby, C. & Eckersley, R. J. In vivo acoustic super-resolution and super-resolved velocity mapping using microbubbles. *IEEE Trans. Med. Imaging.* **34**(2), 433–440 (2015).
28. Desailly, Y., Pierre, J., Couture, O. & Tanter, M. Resolution limits of ultrafast ultrasound localization microscopy. *Phys. Med. Biol.* **60**(22), 8723–8740 (2015).
29. Huang, C. *et al.* Short acquisition time super-resolution ultrasound microvessel imaging via microbubble separation. *Sci. Rep.* **10**(1), 1–13 (2020).
30. Couture, O., Hingot, V., Heiles, B., Muleki-Seya, P. & Tanter, M. Ultrasound localization microscopy and super-resolution: a state of the art. *IEEE Trans. Ultrason. Ferroelectr. Freq. Control* **65**(8), 1304–1320 (2018).
31. Demené, C. *et al.* Transcranial ultrafast ultrasound localization microscopy of brain vasculature in patients. *Nat. Biomed. Eng.* **5**(3), 219–228 (2021).
32. Reference Atlas:: Allen Brain Atlas: Mouse Brain [Internet]. [cited 2021 May 25]. Available from: https://mouse.brain-map.org/static/atlas
33. Song, P., Manduca, A., Trzasko, J. D. & Chen, S. Noise equalization for ultrafast plane wave microvessel imaging. *IEEE Trans. Ultrason. Ferroelectr. Freq. Control.* **64**(11), 1776–1781 (2017).
34. Hingot, V. *et al.* Microvascular flow dictates the compromise between spatial resolution and acquisition time in ultrasound localization microscopy. *Sci. Rep.* **9**(1), 2456 (2019).
35. Christensen-Jeffries, K. *et al.* Poisson statistical model of ultrasound super-resolution imaging acquisition time. *IEEE Trans. Ultrason. Ferroelectr. Freq. Control* **66**(7), 1246–1254 (2019).
36. Lowerison, M. R. *et al.* In vivo confocal imaging of fluorescently labeled microbubbles: implications for ultrasound localization microscopy. *IEEE Trans. Ultrason. Ferroelectr. Freq. Control* **67**(9), 1811–1819 (2020).
37. Shelton, S. E. *et al.* Quantification of microvascular tortuosity during tumor evolution utilizing acoustic angiography. *Ultrasound Med. Biol.* **41**(7), 1896–1904 (2015).
38. Tuma, R. F., Irion, G. L., Vasthare, U. S. & Heinel, L. A. Age-related changes in regional blood flow in the rat. *Am. J. Physiol.* **249**(3 Pt 2), H485-491 (1985).
39. Ollenberger, G. P. & West, N. H. Distribution of regional cerebral blood flow in voluntarily diving rats. *J. Exp. Biol.* **201**(Pt 4), 549–558 (1998).
40. Camargo, E. E. *et al.* The influence of biological and technical factors on the variability of global and regional brain metabolism of 2-[18F]fluoro-2-deoxy-D-glucose. *J. Cereb. Blood Flow Metab.* **12**(2), 281–290 (1992).
41. Gjedde, A., Hansen, A. J. & Siemkowicz, E. Rapid simultaneous determination of regional blood flow and blood-brain glucose transfer in brain of rat. *Acta Physiol. Scand.* **108**(4), 321–330 (1980).
42. Cremer, J. E. & Seville, M. P. Regional brain blood flow, blood volume, and haematocrit values in the adult rat. *J. Cereb. Blood Flow Metab.* **3**(2), 254–256 (1983).
43. Marchal, G. *et al.* Regional cerebral oxygen consumption, blood flow, and blood volume in healthy human aging. *Arch. Neurol.* **49**(10), 1013–1020 (1992).
44. Pantano, P. *et al.* Regional cerebral blood flow and oxygen consumption in human aging. *Stroke* **15**(4), 635–641 (1984).
45. Mitchell, G. F. *et al.* Arterial stiffness, pressure and flow pulsatility and brain structure and function: the Age, Gene/Environment Susceptibility – Reykjavik Study. *Brain* **134**(11), 3398–3407 (2011).
46. Chen, X., Lowerison, M.R., Dong, Z., Sekaran, N.C., Huang, C., & Chen, S. et al. Localization free super-resolution microbubble velocimetry using a long short-term memory neural network [Internet]. 2021 Oct [cited 2021 Oct 7] p. 2021.10.01.462404. Available from: https://www.biorxiv.org/content/10.1101/2021.10.01.462404v1
47. Tang, M.-X. *et al.* Quantitative contrast-enhanced ultrasound imaging: a review of sources of variability. *Interface Focus.* **1**(4), 520–539 (2011).
48. Murugesan, N., Demarest, T. G., Madri, J. A. & Pachter, J. S. Brain regional angiogenic potential at the neurovascular unit during normal aging. *Neurobiol. Aging.* **33**(5), 1004.e1–16 (2012).
49. Faber, J. E. *et al.* Aging causes collateral rarefaction and increased severity of ischemic injury in multiple tissues. *Arterioscler. Thromb. Vasc. Biol.* **31**(8), 1748–1756 (2011).
50. Kang, H.-M., Sohn, I., Jung, J., Jeong, J.-W. & Park, C. Age-related changes in pial arterial structure and blood flow in mice. *Neurobiol. Aging.* **37**, 161–170 (2016).
51. Kitamura, N. *et al.* Beneficial Effects of Estrogen in a Mouse Model of Cerebrovascular Insufficiency. *PLoS ONE* **4**(4), e5159 (2009).
52. He, Z., He, Y. J., Day, A. L. & Simpkins, J. W. Proestrus levels of estradiol during transient global cerebral ischemia improves the histological outcome of the hippocampal CA1 region: perfusion-dependent and-independent mechanisms. *J. Neurol. Sci.* **193**(2), 79–87 (2002).
53. Kaya, E., Sahin, F. K., Köken, G., Köse, M. & Cevrioglu, A. S. Acute effect of intranasal estrogen on cerebral and cerebellar perfusion in postmenopausal women. *Maturitas* **59**(1), 72–82 (2008).
54. Maki, P. M. & Resnick, S. M. Longitudinal effects of estrogen replacement therapy on PET cerebral blood flow and cognition. *Neurobiol. Aging.* **21**(2), 373–383 (2000).
55. Lowerison, M. R., Huang, C., Lucien, F., Chen, S. & Song, P. Ultrasound localization microscopy of renal tumor xenografts in chicken embryo is correlated to hypoxia. *Sci. Rep.* **10**(1), 1–13 (2020).
56. Matta, B. F., Heath, K. J., Tipping, K. & Summors, A. C. Direct cerebral vasodilatory effects of sevoflurane and isoflurane. *Anesthesiology* **91**(3), 677–680 (1999).
57. Bimbard, C., Demene, C., Girard, C., Radtke-Schuller, S., Shamma, S., & Tanter, M. et al. Multi-scale mapping along the auditory hierarchy using high-resolution functional UltraSound in the awake ferret. eLife [Internet]. [cited 2021 May 27];7. Available from: https://www.ncbi.nlm.nih.gov/pmc/articles/PMC6039176/
58. Soulioti, D. E., Espindola, D., Dayton, P. A. & Pinton, G. F. Super-resolution imaging through the human skull. *IEEE Trans. Ultrason. Ferroelectr. Freq. Control.* **67**(1), 25–36 (2020).

59. du Sert, N. P. *et al.* Reporting animal research: explanation and elaboration for the ARRIVE guidelines 2.0. *PLOS Biol.* **18**(7), e3000411 (2020).
60. Huang, C. *et al.* Noninvasive contrast-free 3D evaluation of tumor angiogenesis with ultrasensitive ultrasound microvessel imaging. *Sci. Rep.* **9**(1), 4907 (2019).
61. Desailly, Y. *et al.* Contrast enhanced ultrasound by real-time spatiotemporal filtering of ultrafast images. *Phys. Med. Biol.* **62**(1), 31–42 (2017).
62. Song, P. *et al.* Improved super-resolution ultrasound microvessel imaging with spatiotemporal nonlocal means filtering and bipartite graph-based microbubble tracking. *IEEE Trans. Ultrason. Ferroelectr. Freq. Control.* **65**(2), 149–167 (2018).
63. Song, P., Manduca, A., Trzasko, J. D. & Chen, S. Ultrasound small vessel imaging with block-wise adaptive local clutter filtering. *IEEE Trans. Med. Imaging* **36**(1), 251–262 (2017).
64. Loupas, T., Powers, J. T. & Gill, R. W. An axial velocity estimator for ultrasound blood flow imaging, based on a full evaluation of the Doppler equation by means of a two-dimensional autocorrelation approach. *IEEE Trans. Ultrason. Ferroelectr. Freq. Control* **42**(4), 672–688 (1995).
65. Song, P., Manduca, A., Trzasko, J. D., Daigle, R. E. & Chen, S. On the effects of spatial sampling quantization in super-resolution ultrasound microvessel imaging. *IEEE Trans. Ultrason. Ferroelectr. Freq. Control.* **65**(12), 2264–2276 (2018).
66. Tang, S. *et al.* Kalman filter-based microbubble tracking for robust super-resolution ultrasound microvessel imaging. *IEEE Trans. Ultrason. Ferroelectr. Freq. Control.* **67**(9), 1738–1751 (2020).
67. Jaqaman, K. *et al.* Robust single-particle tracking in live-cell time-lapse sequences. *Nat. Methods* **5**(8), 695–702 (2008).
68. Hobby, J. D. Smooth, easy to compute interpolating splines. *Discrete Comput. Geom.* **1**(2), 123–140 (1986).
69. R Core Team. R: A Language and Environment for Statistical Computing [Internet]. Vienna, Austria: R Foundation for Statistical Computing (2019). Available from: https://www.R-project.org/
70. Wickham, H. *ggplot2: Elegant Graphics for Data Analysis [Internet]* (Springer-Verlag, New York, 2016).

Author contributions

M.L., N.C.S, D.L., and P.S. designed and wrote the paper. N.C.S. and D.L. prepared the mouse model and performed craniotomies. M.L., W.Z., Z.D., and P.S. performed the ultrasound imaging. Z.D. designed the ultrasound transducer holder and programmed the motorized imaging stage. M.L. and N.C.S. performed image segmentation and image analysis. M.L., X.C., and P.S. developed and applied the super-resolution algorithm. Authors were not blinded to animal age cohort.

Funding

The study was partially supported by the National Cancer Institute, the National Institute of Biomedical Imaging and Bioengineering, the National Institute on Deafness and Other Communication Disorders, and the National Institute on Aging of the National Institutes of Health under grant numbers R00CA214523, R21EB030072, R21DC019473 and R03AG059103, as well as a grant to DL from the Kiwanis Neuroscience Research Foundation. The content is solely the responsibility of the authors and does not necessarily represent the official views of the National Institutes of Health. NCS is supported by a Beckman Institute Postdoctoral Fellowship.

Competing interests

The authors declare no competing interests.

Additional information

Supplementary Information The online version contains supplementary material available at https://doi.org/10.1038/s41598-021-04712-8.

Correspondence and requests for materials should be addressed to D.A.L. or P.S.

Reprints and permissions information is available at www.nature.com/reprints.

Publisher's note Springer Nature remains neutral with regard to jurisdictional claims in published maps and institutional affiliations.